Hydrogen Mapping of the Lunar South Pole Using the LRO Neutron Detector Experiment LEND

I. G. Mitrofanov,[1]* A. B. Sanin,[1] W. V. Boynton,[2] G. Chin,[3] J. B. Garvin,[3] D. Golovin,[1]
L. G. Evans,[4] K. Harshman,[2] A. S. Kozyrev,[1] M. L. Litvak,[1] A. Malakhov,[1] E. Mazarico,[3]
T. McClanahan,[3] G. Milikh,[5] M. Mokrousov,[1] G. Nandikotkur,[5] G. A. Neumann,[3] I. Nuzhdin,[1]
R. Sagdeev,[5] V. Shevchenko,[7] V. Shvetsov,[8] D. E. Smith,[9] R. Starr,[6] V. I. Tretyakov,[1]
J. Trombka,[10] D. Usikov,[5] A. Varenikov,[1] A. Vostrukhin,[1] M. T. Zuber[9]

Hydrogen has been inferred to occur in enhanced concentrations within permanently shadowed regions and, hence, the coldest areas of the lunar poles. The Lunar Crater Observation and Sensing Satellite (LCROSS) mission was designed to detect hydrogen-bearing volatiles directly. Neutron flux measurements of the Moon's south polar region from the Lunar Exploration Neutron Detector (LEND) on the Lunar Reconnaissance Orbiter (LRO) spacecraft were used to select the optimal impact site for LCROSS. LEND data show several regions where the epithermal neutron flux from the surface is suppressed, which is indicative of enhanced hydrogen content. These regions are not spatially coincident with permanently shadowed regions of the Moon. The LCROSS impact site inside the Cabeus crater demonstrates the highest hydrogen concentration in the lunar south polar region, corresponding to an estimated content of 0.5 to 4.0% water ice by weight, depending on the thickness of any overlying dry regolith layer. The distribution of hydrogen across the region is consistent with buried water ice from cometary impacts, hydrogen implantation from the solar wind, and/or other as yet unknown sources.

R adar reflection data returned from the Bistatic Radar Experiment conducted by the Clementine spacecraft initially suggested that deposits of pure water ice might exist in permanently shadowed regions (PSRs) near the lunar south pole (1). The lunar surface was subsequently surveyed with the Lunar Prospector Neutron Spectrometer (LPNS) (2). The energy spectrum of neutrons produced by the galactic cosmic ray particles in the uppermost layer (<1 m) of lunar soil carries the imprint of hydrogen, particularly in the epithermal energy range [see the supporting online material (SOM), section 1]. The LPNS observations from its omnidirectional neutron detectors sensors revealed a noticeable suppression of epithermal neutrons around the lunar poles above 70° latitude, which were interpreted to indicate enhancement of hydrogen and/or deposits of water ice, predominantly within PSR areas (3–5).

Here we present data from the Lunar Exploration Neutron Detector (LEND) instrument onboard the NASA Lunar Reconnaissance Orbiter (LRO) (6–9) that provide further information on the distribution of hydrogen in the lunar south pole region and thus a context for interpreting the Lunar Crater Observation and Sensing Satellite (LCROSS)

[1]Institute for Space Research of the Russian Academy of Science, 117997 Moscow, Russia. [2]University of Arizona, Tucson, AZ, USA. [3]NASA Goddard Space Flight Center, Greenbelt, MD, USA. [4]Computer Science Corporation, Greenbelt, MD, USA. [5]Department of Physics, University of Maryland, College Park, MD, USA. [6]Catholic University, Washington, DC, USA. [7]Sternberg Astronomical Institute of Moscow State University, Moscow, Russia. [8]Joint Institute of Nuclear Research, Dubna, Russia. [9]Massachusetts Institute of Technology, Cambridge, MA, USA. [10]Department of Astronomy, University of Maryland, College Park, MD, USA.

*To whom correspondence should be addressed. E-mail: imitrofa@space.ru

experimental results. The LEND epithermal neutron detectors are surrounded by a collimator, which provides them with a narrow field of view (FOV) corresponding to a spatial resolution of ~10 km [full width at half maximum (FWHM)] on the lunar surface from the nominal lunar orbit of 50 km [(10) and SOM, section 2]. Initial LEND data obtained from July until September 2009 were used in the selection of the target for the LCROSS impact (SOM, section 3), in conjunction with the LRO Lunar Orbiter Laser Altimeter (LOLA) altimetry data (11). The target named SP_C within Cabeus crater was selected for the final LCROSS impact (12) from among several sites (SOM, section 3), partly on the basis of the LEND neutron measurements. Here we include and discuss data obtained from 3 July 2009 to 25 July 2010. This ~1-year time interval provides for statistically robust neutron counting statistics for the lunar south polar region and allows an assessment of the following two questions: (i) What is the difference in hydrogen content at specific PSRs in comparison with that in sunlit areas at a similar latitude? (ii) How large is the difference between the observed hydrogen content at the specific PSRs in question and that in a general reference area outside of the southern polar region?

In order to estimate the hydrogen content of the regolith that is responsible for the observed suppressed neutron fluxes, we normalized the neutron count rates to a location of well-established hydrogen content. On the basis of an analysis of LPNS data, the minimum hydrogen concentration across the entire lunar surface is 10 to 50 parts per million (ppm) (3, 4). A similar value was measured in Apollo lunar soil samples (13). Therefore, we assume a minimum reference value of 10 ppm for the bulk lunar regolith hydrogen

content in the latitude belt from 60° to 70°S, just outside the extended area of polar epithermal neutron suppression. The corresponding neutron flux is at a count rate, r_0, of about 1.9 counts per second (cps) within the instrument FOV from the sum of all four collimated LEND detectors [SOM, section 6, and (14, 15)]. All of the nine PSRs in question have surface areas (Table 1) that are larger than or comparable to the area of the LEND instrument FOV, and, as a first approximation, we therefore attribute the measured difference Δr of the count rates for them to the suppression of the neutron flux by hydrogen in the evaluated targets. In this case, the dimensionless total suppression parameter for any tested PSR site may be defined as $\xi = 1 - \Delta r/r_0$ (no suppression corresponds to $\xi = 1$, and full suppression corresponds to $\xi = 0$). The measurement error associated with this parameter can be directly computed from the statistical variability of the counts used in the estimation of Δr (Table 1) and from the uncertainty in the value of r_0. On the basis of LEND data collected during the LRO cruise phase and model calculations, the value of r_0 could potentially be as low as 1.5 cps, as the lowest limit supported by data (SOM, section 6). We use the value of 1.9 cps for our estimates below, which will serve to bound the smallest possible value of hydrogen content and could therefore be considered to be a conservative lower limit [see also (16)].

To investigate the question (i) whether the PSRs contain significantly more hydrogen than any nearby sunlit area, we measured the difference Δr_{loc} between the epithermal neutron count rate at each of nine tested PSRs and the count rate for the sunlit (non-PSR) surface of a 360° band with the same latitude as that of the PSR (second column of Table 1) (SOM, section 4). Only two of the nine PSRs, Shoemaker (case 2 of Table 1) and Cabeus (case 3 in Table 1), show a statistically significant decrease of the neutron flux, with corresponding local suppression parameters $\xi_{loc} = (1 - \Delta r_{loc}/r_0)$ of ~0.95 and 0.85, respectively. The specific counting statistics for the seven remaining PSRs were inadequate for statistically robust measurements of their local neutron suppressions, but do facilitate the establishment of lower limits for parameters associated with local neutron suppression, as $\xi_{lim} = 1 - 3\sigma/r_0$. For example, in three specific cases (4, 5, and 7 in Table 1) they are >0.8. In two other cases [1 and 5 in Table 1 (Faustini and Haworth)], statistics permit the estimation of more conservative lower limits for the local suppression parameters, corresponding to 0.92 and 0.96, respectively. Lower limits of neutron suppression parameters ξ_{lim} between 0.96 and 0.80 correspond to relatively small upper limits for hydrogen enhancement in the evaluated PSRs of ~100 and 500 ppm, respectively (fig. S1 of SOM, section 1). The total cumulative surface area of all lunar PSRs constitutes only a few percent of the sunlit surface area within the lunar poles, and with such a small enhancement of hydrogen, they would not be expected to de-

crease the outgoing flux of epithermal neutrons as a mechanism to explain the observed extended neutron suppression around lunar poles.

To address question (ii), we compared the average LEND count rates of the nine PSRs with the average count rate at a single southern-latitude reference belt from 60° to 70°S (third column of Table 1). This belt is located outside the polar epithermal suppression band and its average neutron flux is 5.095 ± 0.002 cps. Only three of the nine PSRs (Shoemaker, Cabeus, and Haworth) had a statistically significant decrease in their neutron flux in comparison with that of the reference belt; one PSR (Faustini, case 1 in Table 1) displays a marginally significant decrease of its neutron flux (Table 1). Site SP_C within the Cabeus PSR (case 3 in Table 1) displayed the strongest total suppression effect of about 0.33 ± 0.09 cps among all of the nine PSR targets. This result confirms the selection of this site for the actual LCROSS impact on the basis of its enhanced hydrogen content.

A contour map of the epithermal neutron flux (shown as pink in Fig. 1) delineates the neutron suppression region (NSR) within Cabeus (SOM, section 5). The difference between the outermost contour that defines the boundary of the region and the deepest inner part is ~0.10 cps (compare cases 10 and 11 in Table 1). It is evident that the southern part of the NSR extends beyond the PSR boundary toward the pole by up to about 20 km, and the region of greatest suppression (inner pink contour in Fig. 1) is also offset from the outline of the PSR. Furthermore, the subsurface temperature across the region with suppressed neutron emission, and not only within the PSR, is approximately 60 K, as measured by the LRO's Diviner Lunar Radiometer (17) (Fig. 1, insert). The LEND neutron data demonstrate the occurrence of local NSRs at the lunar poles, which are located both within PSRs and within sunlit regions.

The PSR within Shoemaker (case 2 in Table 1) has the largest area and a favorable south polar location for the accumulation of LEND counting statistics; thus, the total suppression parameter for this site is the most significant at 7.3σ, but its value of 0.918 ± 0.011 is still relatively small (column 4 in Table 1). The corresponding hydrogen content is estimated at 200 ppm (fig. S1 of SOM, section 1). The PSR site SP_C within Cabeus (case 3 of Table 1) displays the strongest total neutron suppression parameter, 0.825 ± 0.047, among all of the sites, and thus the highest estimated hydrogen content of ~470 ppm. The average total neutron suppression parameter within the NSR associated with the entire Cabeus crater is 0.875 ± 0.023 (case 10 of Table 1), suggesting a hydrogen content of about 300 ppm. The central area of the NSR (innermost pink contour, Fig. 1), displays a suppression of 0.82 ± 0.07 (case 11 in Table 1) and thus an estimated hydrogen content of about 500 ppm. However, this value is only marginally significant, corresponding to 2.5σ with respect to the reference latitude band.

The presence of the Cabeus NSR outside the boundary of the topographically defined PSR

Table 1. Effects of the suppression of the epithermal neutron count rate within the nine PSRs from the list of LCROSS candidate impact sites and within the NSR associated with Cabeus crater (first column). Derived LEND counts for these sites are given in table S2 in section 4 of the SOM. Corresponding names and coordinates according to the LCROSS candidate impact sites are given in table S1 in section 3 of the SOM. The local neutron suppression effect is given in the second column as the difference Δr_{loc} between the average counting rate of the non-PSR (sunlit) region at the latitude of the PSR and the counting rate in the tested PSR region (see column 8 of table S2 in section 4 of the SOM). The total suppression effect is given in the third column as the difference Δr between the average counting rate in the low-hydrogen southern-latitude band at 60° to 70°S and the neutron counting rate in the tested region (see column 9 of table S2 in section 4 of the SOM). The total suppression parameter is given in the fourth column, as $\xi = 1 - \Delta r/r_0$ with respect to the reference value $r_0 = 1.9$ cps of collimated flux at a low-hydrogen region at latitudes between 60° and 70°S. Uncertainties of dimensionless suppression ξ are estimated by dividing the error of Δr by the reference value r_0.

Name and area of region	Local neutron suppression Δr_{loc} (cps)	Total neutron suppression Δr (cps)	Total suppression parameter $\xi = 1 - \Delta r/r_0$
1. PSR Faustini (SP_A), 635 km²	0.05 ± 0.05 (1.0σ)	0.12 ± 0.05 (2.4σ)	0.936 ± 0.027
2. PSR Shoemaker (SP_B), 1048 km²	0.089 ± 0.022 (4.0σ)	0.156 ± 0.021 (7.3σ)	0.918 ± 0.011
3. PSR Cabeus (SP_C), 243 km²	0.28 ± 0.09 (3.1σ)	0.33 ± 0.09 (3.7σ)	0.825 ± 0.047
4. PSR Cabeus B1 (SP_CB), 342 km²	-0.01 ± 0.10 (-0.07σ)	0.02 ± 0.10 (0.2σ)	Not significant
5. PSR Cabeus-2 (SP_CC), 121 km²	0.04 ± 0.14 (0.3σ)	0.10 ± 0.14 (0.7σ)	Not significant
6. PSR Haworth (SP_D), 973 km²	0.012 ± 0.027 (0.4σ)	0.08 ± 0.026 (3.0σ)	0.958 ± 0.014
7. PSR Malapert F1 (SP_F), 264 km²	0.01 ± 0.11 (0.1σ)	0.05 ± 0.11 (0.5σ)	Not significant
8. PSR Malapert-2 (SP_G), 77 km²	-0.35 ± 0.18 (-2.0σ)	-0.29 ± 0.18 (-1.6σ)	Not significant
9. PSR Cabeus A1 (SP_CA), 59 km²	0.07 ± 0.27 (0.3σ)	0.09 ± 0.27 (0.3σ)	Not significant
10. NSR at Cabeus, 718 km²	–	0.24 ± 0.05 (5.3σ)	0.875 ± 0.023
11. Center part of NSR at Cabeus, 76 km²	–	0.34 ± 0.14 (2.5σ)	0.82 ± 0.07

(Fig. 1) has implications for understanding the origin of enhanced hydrogen concentrations in the lunar polar regions. In sunlit areas near the lunar poles, the upper few centimeters of the soil could be heated to ~200 K (17). Hydrogen-rich volatiles (such as water ice) should leak out at these temperatures; thus, this surface layer should have a much smaller hydrogen content than the soil below (18, 19). The estimates of hydrogen content in Table 1 were computed assuming that hydrogen was distributed uniformly with depth (SOM, section 1), but if there is a drier (i.e., hydrogen-poor) overlying layer with 100 ppm of hydrogen, then the hydrogen content at depth will be significantly higher. For example, for a 40-, 50-, or 60-cm-thick overlying layer and for a bulk regolith density of 1.6 g/cm³, we would estimate that a buried soil layer in the Cabeus NSR could have a hydrogen content of ~600, 1200, or 4500 ppm, respectively. The final value corresponds to a water (as ice) content of ~4% by weight, which is in good agreement with independent estimates of the water content asso-

ciated with the LCROSS Centaur impact site of $5.6 \pm 2.9\%$ by weight (12).

Because of the similarity of the neutron suppression and temperature in both shadowed and sunlit areas of the NSR (Fig. 1), which suggests a similar deposition of hydrogen in the shallow subsurface, a more complex model of volatile accumulation in the lunar polar regolith is required than simple cold-trapping of water molecules exclusively within PSRs. We suggest that a layer buried beneath a drier surface layer is enriched in hydrogen, and that these layers extend through both illuminated and permanently shadowed surfaces in the floor of Cabeus crater. This hypothesis is similar to that which has been considered to apply to the polar regions of Mars (20, 21). Suggested origins of the hydrogen include implantation of solar wind protons; condensation of transient water-rich atmospheres from cometary impacts, modified by gardening by micrometeorites; and space weathering (22, 23). More data is necessary from LRO to develop and test this hypothesis (24).
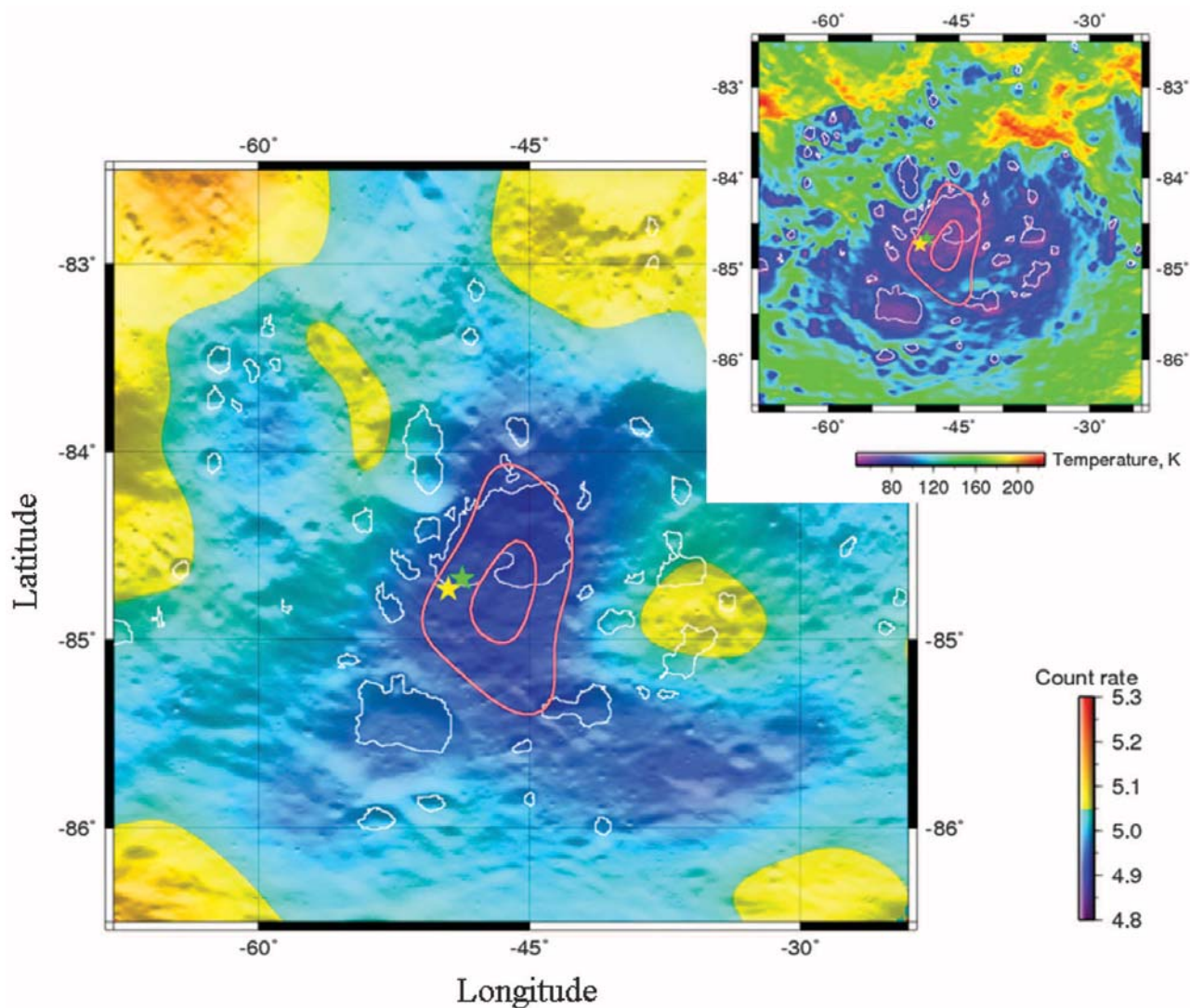
Fig. 1. LEND-derived map of the epithermal neutron flux within Cabeus crater (primary cavity). Colors represent the level of epithermal neutron flux (cps). The map is smoothed by a Gaussian filter with a 14-km scale (1σ). The thin white contours outline the boundaries of PSRs according to best-available LOLA altimetry. The outermost pink contour represents the statistically most likely boundary of the NSR within the Cabeus crater, and the innermost pink contour represents the region of strongest neutron suppression within the NSR (cases 10 and 11 of Table 1, respectively, and SOM, section 5). The colored stars represent the locations of the LCROSS impact sites (green and yellow correspond to the Shepherding Spacecraft and the Centaur upper stage, respectively). The insert (upper right) represents the map of subsurface temperatures within Cabeus from the LRO Diviner instrument (17); the contours associated with the LOLA-defined PSRs and LEND-defined NSR are also shown on this inset temperature map (upper right).

References and Notes

1. P. D. Spudis et al., Sol. Syst. Res. **32**, 17 (1998).
2. W. C. Feldman et al., Nucl. Instrum. Methods Phys. Res. **422**, 562 (1999).
3. W. C. Feldman et al., Science **281**, 1496 (1998).
4. D. J. Lawrence et al., J. Geophys. Res. **111**, E08001 (2006).
5. R. C. Elphic et al., Geophys. Res. Lett. **34**, L13204 (2007).
6. G. Chin et al., Space Sci. Rev. **129**, 391 (2007).
7. R. R. Vondrak, J. Keller, G. Chin, J. Garvin, Space Sci. Rev. **150**, 7 (2010).
8. I. G. Mitrofanov et al., Astrobiol. **8**, 793 (2008).
9. I. G. Mitrofanov et al., Space Sci. Rev. **150**, 183 (2010).
10. The LEND spatial resolution is a function of LRO spacecraft orbital altitude. The value of 10 km is the physical resolution of the instrument at an orbital altitude of 50 km (FWHM). This scale corresponds to an area of about 75 km² on the lunar surface. The resolution scale is inversely proportional to the orbital altitude. Over the course of the LRO mission, the altitude varied from ~30 to ~70 km (with an average of ~50 km), and the exact values at any given time are available in the Planetary Data System. The precise value of the spatial resolution is not critical to the primary conclusions of this work, as we are investigating differences in neutron count rates for PSR sites and reference regions that are larger than (or comparable to) the area of a typical LEND-resolution element or footprint (Table 1). The tested PSR target in Cabeus known as SP-C has an area of 243 km², which is larger by a factor of at least 4 than the area of a LEND-resolution element for all representative operational LRO spacecraft altitudes. Obviously, the larger the spatial resolution of the instrument surface FOV, the more difficult it will be to reliably measure contrasts in the neutron count rate. When maps are constructed from such data, the spatial resolution is also a function of the amount of spatial smoothing needed to reduce the random noise. To construct the LEND neutron counting rate map illustrated in Fig. 1, the data were Gaussian-smoothed with a spatial scale of 14 km (1σ). However, spatially smoothed data were not used for measuring the average neutron count rate for the tested targets. Additional details can be found in the SOM, section 2.
11. M. T. Zuber et al., Space Sci. Rev. **150**, 63 (2010).
12. A. Colaprete et al., Science **330**, 463 (2010).
13. G. H. Heiken, D. T. Vaniman, V. M. French, Lunar Sourcebook: A User's Guide to the Moon (Cambridge Univ. Press, New York, 1991).
14. D. J. Lawrence, R. C. Elphic, W. C. Feldman, H. O. Funsten, T. H. Prettyman, Astrobiology **10**, 183 (2010).
15. LEND flight mission data support the use of 1.9 cps as the reference neutron flux, in spite of recently published results (14) that suggest much lower values on the basis of independent models of the LEND instrument and assumptions about the design of its collimator. Lower values for the neutron flux suggested in (14) would result in neutron suppression values of over 50% around the lunar poles, which are far larger than those already measured by the LPNS (2).
16. One can readily convert our estimates for the absolute suppression parameter (column 4 in Table 1) from the baseline case of $r_0 = 1.9$ cps to the lower limit case of 1.5 cps, using the expression for this parameter. In this case, the suppression curve illustrated in fig. S1 (SOM, section 1)

could be used with new estimates of the suppression parameter to yield appreciably larger estimates of the hydrogen content in the shallow lunar subsurface.
17. D. A. Paige *et al.*, *Science* **330**, 479 (2010).
18. J. R. Salvail, F. P. Fanale, *Icarus* **111**, 441 (1994).
19. A. R. Vasavada, D. A. Paige, S. E. Wood, *Icarus* **141**, 179 (1999).
20. W. V. Boynton *et al.*, *Science* **297**, 81 (2002).
21. I. Mitrofanov *et al.*, *Science* **297**, 78 (2002).
22. D. H. Crider, R. R. Vondrak, *J. Geophys. Res.* **108**, 5079 (2003).
23. D. H. Crider, R. R. Vondrak, *Adv. Space Res.* **31**, 2293 (2003).
24. The LRO Mission is supported by the NASA Exploration System Mission Directorate, and the LEND investigation is supported by the Russian Federal Space Agency. We acknowledge the LRO Project team at NASA's Goddard Space Flight Center for their outstanding support of the LEND investigation.

A New Mixing Diagnostic and Gulf Oil Spill Movement

Igor Mezić,[1]* S. Loire,[1]† Vladimir A. Fonoberov,[2]† P. Hogan[3]

Chaotic advection has served as the paradigm for mixing in fluid flows with simple time dependence. Its skeletal structure is based on analysis of invariant attracting and repelling manifolds in fluid flows. Here we develop a finite-time theory for two-dimensional incompressible fluid flows with arbitrary time dependence and introduce a new mixing diagnostic based on it. Besides stretching events around attracting and repelling manifolds, this allows us to detect hyperbolic mixing zones. We used the new diagnostic to forecast the spatial location and timing of oil washing ashore in Plaquemines Parish and Grand Isle, Louisiana, and Pensacola, Florida, in May 2010 and the flow of oil toward Panama City Beach, Florida, in June 2010.

Chaotic advection theory (*1–3*) explains the phenomenon of mixing behavior in fluid flows with simple time dependence. This is achieved using hyperbolicity concepts associated with attracting and repelling lines, as well as hyperbolic zones with strongly chaotic behavior (*4*). However, chaotic advection and mixing phenomenology in that case depend on the recurrence of hyperbolic behavior and thus are difficult to extend to analyze flows with complex time dependence, such as those occurring in the ocean and atmosphere. Detecting geometric structures has become increasingly important in analyzing fluid flows with complex time dependence because of the realization that even turbulent flows feature Lagrangian structures that can be understood from the perspective of finite-time dynamical systems theory (*5–7*). This has led to the development of the theory of Lagrangian coherent structures (*8*), within which researchers focused on finite-time behavior, such as finding the attracting or repelling finite-time invariant curves (*5, 6, 9, 10*). In (*11*), an alternative approach stems from studies of the statistical properties of dynamical systems, showing that Lagrangian time-averages of physically relevant functions on state space enable the detection of invariant sets of dynamical systems, including experimentally realizable fluid flows with simple time dependence (*12–14*). Here we develop this theory further, based on the gradient of the average Lagrangian velocity field.

Consider the time evolution of a fluid flow on time interval $\tau = [t_0, t_0 + T]$. The dynamics of fluid particles in an incompressible two-dimensional (2D) flow on a domain $A \subset R^2$ is given by

$$\dot{\mathbf{x}} = \mathbf{v}(\mathbf{x}, t) \qquad (1)$$
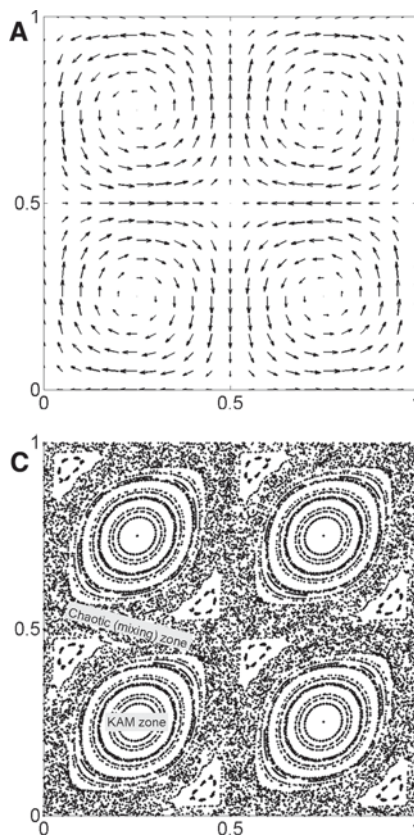
where $\nabla \cdot \mathbf{v} = 0$. The position of the fluid particle starting at time t_0 at a cartesian spatial location $\mathbf{x}_0 = (x_0, y_0)$ moves to $(x(t_0 + T, x_0, y_0, t_0), y(t_0 + T, x_0, y_0, t_0))$ at time $t_0 + T$

$$x(t_0 + T, x_0, y_0, t_0) = x_0 + \int_{t_0}^{t_0+T} v_x(t, x(t_0 + t, x_0, y_0, t_0), y(t_0 + t, x_0, y_0, t_0))dt \qquad (2)$$

$$y(t_0 + T, x_0, y_0, t_0) = y_0 + \int_{t_0}^{t_0+T} v_y(t, x(t_0 + t, x_0, y_0, t_0), y(t_0 + t, x_0, y_0, t_0))dt \qquad (3)$$

If we denote by $\mathbf{v}^*(\mathbf{x}_0, t_0, T) = (v_x^*(x_0, y_0, t_0, T), v_y^*(x_0, y_0, t_0, T))$ the average Lagrangian velocity on τ starting from $\mathbf{x}_0$, we have

$$x(t_0 + T, x_0, y_0, t_0) = x_0 + T v_x^*(x_0, y_0, t_0, T) \qquad (4)$$

$$y(t_0 + T, x_0, y_0, t_0) = y_0 + T v_y^*(x_0, y_0, t_0, T) \qquad (5)$$

Fig. 1. (**A**) A cellular, divergence-free velocity field described in Eq. 6. (**B**) Hypergraph map for the velocity field shown in (A), for $T = 0.94248$. (**C**) Poincaré map for the time-periodic, divergence-free perturbation of the velocity field shown in (A) by a vector field described in Eq. 7, with $\varepsilon = 0.1$. (**D**) Hypergraph map for the time-periodic velocity field whose Poincaré map is shown in (C), for $T = \pi$.

[1]Center for Control, Dynamical Systems and Computation, and Department of Mechanical Engineering, University of California, Santa Barbara, CA 93106, USA. [2]Aimdyn, Santa Barbara, CA 93101, USA. [3]Naval Research Laboratory, Stennis Space Center, MS 39529, USA.

*To whom correspondence should be addressed. E-mail: mezic@engineering.ucsb.edu
†These authors contributed equally to this work.